



Hybrid assessment of acoustic radiation damping combining in-situ mobility measurements and the boundary element method

Suhaib Koji Baydoun^{1,*}, N.B. Roozen^{1,2}, and Steffen Marburg¹

¹Technical University of Munich, TUM School of Engineering and Design, Chair of Vibroacoustics of Vehicles and Machines, Boltzmannstraße 15, 85748 Garching, Germany

²KU Leuven, Laboratory of Acoustics, Soft Matter and Biophysics, Department of Physics and Astronomy, Celestijnenlaan 200D, Leuven 3001, Belgium

Received 28 April 2022, Accepted 2 September 2022

Abstract – A hybrid experimental-numerical approach is proposed for assessing acoustic radiation damping – a major energy dissipating mechanism in lightweight structures. The vibrational behavior is characterized by distributed mobility measurements using laser Doppler vibrometry allowing to realistically capture the mechanical behavior of the structure under test. The experimentally obtained matrix of mobilities are coupled to a boundary element model to evaluate the radiated sound power numerically. Thereby, acoustic measurements and associated low frequency limitations are avoided, which results in two salient features of the proposed hybrid approach: modeling of diffuse incident acoustic fields and consideration of acoustic short-circuiting induced by slits and gaps. These features contribute to an accurate and excitation-dependent estimation of acoustic radiation damping in the low frequency range. The proposed hybrid approach is applied to flat and C-shaped aluminum sandwich panels mounted onto a tub-shaped foundation. The results are compared to those obtained by a previously reported numerical method.

Keywords: Boundary element method, Acoustic radiation damping, Laser Doppler vibrometry

1 Introduction

Composite structures such as honeycomb sandwich panels exhibit excellent elastic properties but only low material inherent damping. The latter issue is addressed extensively by material scientists and engineers with a view to mitigate unwanted vibrations by means of passive and active damping devices. Clearly, an effective design of such damping treatments requires accurate quantification of damping in the first place [1]. In fact, accurate quantification of different damping contributions is an essential aspect in the design process of lightweight structures. An important and yet often neglected damping contribution in lightweight structures is known as *acoustic radiation damping* [2]. It refers to the energy dissipation of vibrating structures due to far-field sound radiation.

The earliest and perhaps most straight forward approach for assessing radiation damping is based on in-vacuo reference measurements [3, 4]. Clarkson and Brown deduced damping values of a honeycomb sandwich panel by relating the input power of a shaker to the average vibrational velocity [3]. By conducting the same experiments in air and in-vacuo, they were able to distinguish between

acoustic radiation damping and material inherent damping of the panel. Zhou and Crocker followed a different approach and determined radiation damping of sandwich panels clamped in a window between two reverberation rooms by measuring both the surface velocity and the sound pressure in the receiving room [5].

In contrast to numerical modeling, such experiments allow to properly capture the elastic behavior of structures involving complex material configurations. This is an important aspect since radiation damping is particularly relevant in lightweight structures that are designed to achieve a high ratio of bending stiffness to mass. However, in the majority of the cases, experimental set-ups imply significant limitations on the specimen's geometry and also on the boundary conditions, which make in-situ measurements difficult. For example, a vacuum chamber needs to be large enough to accommodate the specimen, and it can be cumbersome to access all surfaces by laser Doppler vibrometry (LDV) in order to measure the vibration levels. Moreover, excitation by incident acoustic fields is not possible, although radiation damping strongly depends on the type of excitation at low frequencies.

Similar restrictions hold for sound transmission facilities, which limit the geometry of the specimen to the shape of the window cut-out between the two rooms. Moreover,

*Corresponding author: suhaib.baydoun@tum.de

the clamping inside the window hardly resembles the actual mounting condition, which can falsify the dynamic response at low frequencies. Indeed, acoustic measurements are generally subject to large uncertainties in the low frequency range: Measurements inside reverberation rooms are based on the assumption of diffuse acoustic fields, which become invalid due to the modal behavior of the room [6], and the effectiveness of absorbent treatments in anechoic chambers is also limited below the cut-off frequency [7].

Besides experimental approaches, radiation damping can be estimated numerically based on a vibroacoustic simulation model. In our previous work, the finite (FEM) and the boundary element method (BEM) were combined with a nonlinear eigensolver in order to derive radiation damping values corresponding to certain structural modes [8]. The main advantage of that numerical approach compared to the above mentioned experimental methods is that the acoustic conditions and associated effects such as scattering and short-circuiting can be accurately modeled even at low frequencies. Further, the coupled FEM–BEM approach allows to capture the modal behavior of the structure and thus the excitation dependence of radiation damping. However, the corresponding eigenfrequencies depend on the actual boundary conditions, which can hardly be reproduced in a simulation. Usually, idealized boundary conditions are employed in finite element models such as *clamped* or *simply supported*. Often, it is difficult to tell which of these conditions resembles the actual configuration, and indeed the truth in many cases lies somewhere in between. Inaccurately modeled boundary conditions can subject acoustic quantities to large errors when sound radiation is mainly driven by edge and corner motions. Moreover, prestress occurring in assembled components can have implications on sound radiation as well, but is difficult to accurately model in simulations.

The uncertainty associated with boundary conditions, excitation and acoustic measurements in the low frequency range is illustrated in Figure 1, which shows radiation damping values of a foam-filled honeycomb sandwich panel. The experimental values are taken from the literature [5] and were obtained by the authors in a window test rig between two reverberation rooms using shaker excitation. Figure 1 compares those experimental values to theoretical estimates [9, 10] based on principles of power flow as well as to radiation damping values computed by the FEM–BEM approach assuming an infinitely extended acoustic baffle and five randomly positioned point forces as excitation. All three methods show good agreement to each other in the higher frequency range above coincidence, which occurs around 780 Hz. However, we also observe significant deviations in the lower frequency range where the modes of the panel are widely separated and radiation damping strongly depends on the excitation. The deviation between the experimental and the numerical results are likely attributed to the effect of boundary conditions, the excitation and also to the low modal density of the reverberation rooms. Our conclusion is that reliable methods for predicting radiation damping in the low frequency range are currently not available.

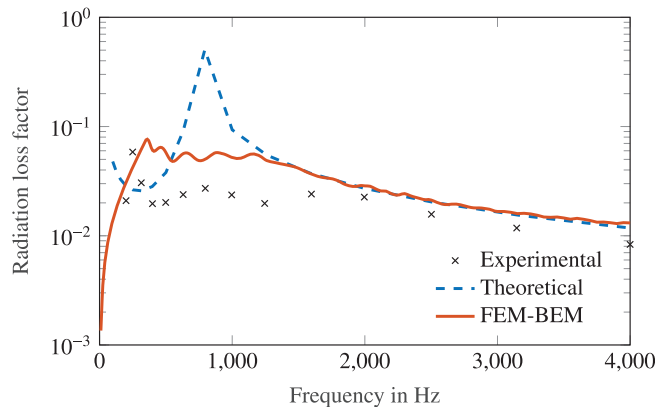


Figure 1. Radiation loss factors of a sandwich panel with foam-filled honeycomb core. Comparison of experimental values taken from the literature [5] to theoretical estimates as well as to numerical results obtained by a FEM–BEM approach.

The uncertainties related to boundary conditions, excitation and diffuse acoustic fields in the low frequency range are widely addressed in literature – not exactly with regard to acoustic radiation damping but in the context of sound transmission loss [11–14]. Different to radiation damping, which is a generally relevant aspect in lightly damped structures, sound transmission analysis only applies to partitions between sending and receiving rooms and does not require measuring the structural response.

Usually, researchers focus on either experimental or numerical methods and then use the respectively other one for the purpose of verification. However, as discussed above, both approaches exhibit shortcomings that are of different origins. An intuitive and yet often overlooked alternative is to combine the advantages of numerical and experimental methods in a hybrid approach. Examples in the literature include fitting the equations of motions with respect to measured transfer functions [15] and experimental-numerical evaluation of sound radiation of a boat hull [16]. Shephard et al. combined an experimental modal analysis with a lumped parameter model for the representation of underwater sound radiation [17]. In this way, the authors were able to numerically include the effect of added mass after performing the measurements in air. A similar approach has been studied in the context of active control by using simulated measurement data and the boundary element method [18]. More recently, Roozen et al. [19] characterized sound transmission by means of mobility measurements and the Rayleigh integral method – an approach that may be categorized as vibration-based sound power measurement [20, 21].

In this work, we propose a combined experimental-numerical procedure, which extends the currently available methods for assessing radiation damping to the low frequency range. On the one hand, we characterize the dynamical behavior of complex materials by an experimental method – ideally even in the actual mounting condition. On the other hand, we avoid acoustic measurements and associated limitations and instead, employ the boundary element method (BEM) [22] to characterize the acoustic

field. For our purpose of evaluating damping by far-field sound radiation, BEM is particularly appealing because it does not require special treatments for modeling unbounded acoustic domains. Moreover, in comparison to analytical evaluation of sound radiation [19], the use of BEM allows to consider complex geometries as well as acoustic short circuiting induced by slits and gaps. The latter plays a significant role in the sound insulation and radiation at low frequencies [23, 24], which will be demonstrated later in this paper. The proposed hybrid framework contributes to an accurate low-frequency assessment of acoustic radiation damping covering the following aspects:

- Firstly, the dynamic response is evaluated by taking the actual mounting condition into account, thus avoiding idealized mechanical boundary conditions.
- Secondly, the actual acoustic field and associated effects such as scattering and short-circuiting are considered without the need of acoustic measurement facilities.
- Lastly, radiation damping can be evaluated under any excitation including diffuse incident fields.

The paper is organized as follows. Section 2 describes the experimental-numerical framework and provides details regarding the coupling, the modeling of diffuse incident fields and the evaluation of radiation damping. The procedure is applied in Sections 3 and 4 to flat and curved honeycomb sandwich panels. The influences of excitation and acoustic conditions on radiation damping in the low frequency range are investigated and the results are compared to those obtained by a previously reported numerical method. The paper concludes in Section 5 with a summary of the main findings and a discussion of future applications and studies.

2 Combined experimental-numerical evaluation of vibroacoustic responses

Despite the above-discussed drawbacks at low frequencies, experimental assessment of radiation damping offers several advantages compared to a purely numerical assessment. The behavior of complex materials is properly taken into account, and when the measurements are conducted in the actual mounting condition, even the effect of the mechanical boundary conditions can be realistically addressed. In this work, we exploit these advantages and characterize the dynamical behavior of structures by an experimental procedure. The structural response is given by

$$\mathbf{v}_r = \mathbf{Y}(\omega)[\mathbf{f}_s + \mathbf{f}_i], \quad (1)$$

in which $\mathbf{Y}(\omega) \in \mathbb{C}^{n_r \times n_e}$ is the experimentally determined matrix of mobilities relating the force excitation to the surface velocity. The angular frequency is defined as $\omega = 2\pi f$. We consider the general case in which the vector $\mathbf{v}_r \in \mathbb{C}^{n_r}$ contains three velocity degrees of freedom (DOF) for each node on the response grid – that is one velocity DOF for each spatial dimension. The same applies to the excitation vector in square brackets on the right-hand

side of equation (1), which is defined on a (possibly different) excitation grid. It comprises structural excitation $\mathbf{f}_s \in \mathbb{C}^{n_e}$ as well as excitation $\mathbf{f}_i \in \mathbb{C}^{n_e}$ by an incident acoustic field.

The acoustic field, which comprises incident and scattered sound waves, is described by the Helmholtz equation and evaluated numerically, thus avoiding the use of acoustic measurement facilities and associated limitations. In the context of this work, mainly unbounded acoustic domains are of interest, since acoustic radiation damping is associated with far-field sound radiation. In this regard, BEM [22] is particularly well-suited for solving the Helmholtz equation, since it does not require special treatments for truncating the far-field sound radiation. Reformulation of the Helmholtz equation by the Kirchhoff integral theorem and subsequent discretization by direct collocation BEM yields the linear system of equations [25]

$$\mathbf{H}\mathbf{p} = \mathbf{G}(\mathbf{v}_f - \mathbf{v}_f^i) + \mathbf{H}\mathbf{p}^i. \quad (2)$$

The vectors $\mathbf{p} \in \mathbb{C}^{n_f}$ and $\mathbf{v}_f \in \mathbb{C}^{n_f}$ contain the complete sound pressure and fluid particle velocities, i.e., the sum of the respective incident and scattered fields. The coefficient matrices \mathbf{H} and \mathbf{G} are fully populated and frequency dependent. Acoustic sources are considered by the incident sound pressure \mathbf{p}^i and the corresponding incident particle velocity \mathbf{v}_f^i .

The fluid loading on the structure can be expressed by the coupling condition

$$\mathbf{f}_f = \mathbf{C}_{ef}\mathbf{p}, \quad (3)$$

where the coupling matrix $\mathbf{C}_{ef} \in \mathbb{R}^{n_e \times n_f}$ relates the acoustic quantities on the BE mesh to the excitation grid. Its computation is presented in Section 2.1. Substituting equation (2) into equation (3) yields

$$\mathbf{f}_f = \mathbf{C}_{ef}\mathbf{H}^{-1}\mathbf{G}\mathbf{v}_f + \underbrace{\mathbf{C}_{ef}(\mathbf{p}^i - \mathbf{H}^{-1}\mathbf{G}\mathbf{v}_f^i)}_{\mathbf{f}_i}. \quad (4)$$

The first term on the right-hand side of equation (4) can be interpreted as a reaction force acting on the structure by virtue of the acoustic field. It includes the effects of radiation damping and added mass, which are included in the measured mobility matrix $\mathbf{Y}(\omega)$ in equation (1). The second term on the right-hand side is the excitation force due to the incident acoustic field. It equals the force vector \mathbf{f}_i on the right-hand side of equation (1). Once the structural velocity \mathbf{v}_r is evaluated for a given excitation, the fluid particle velocity is obtained by the continuity condition

$$\mathbf{v}_f = \mathbf{C}_{fr}\mathbf{v}_r, \quad (5)$$

where the matrix $\mathbf{C}_{fr} \in \mathbb{R}^{n_f \times n_r}$ establishes the coupling between the experimental response grid and the BE nodes. Finally, the sound pressure field can be computed via equation (2).

The proposed hybrid procedure can be incorporated into the design process once subcomponents or prototypes

are available. For example, in-situ mobility measurements could be conducted on a prototype hull of a transport vehicle, and the results could in turn be used to assess the acoustic loading transmitted to the inside. Once the mobility matrix $\mathbf{Y}(\omega)$ is determined, the acoustic response to different excitations can be computed without repeating the experiments. As we will see in [Section 2.2](#), even the response to diffuse incident fields can be computed in the low frequency range without need of special facilities.

But of course, these advantages come at the cost of experimentally determining the mobility matrix $\mathbf{Y}(\omega)$ of a possibly three-dimensional, large scale structure. While the associated effort may have been prohibitive a decade ago, nowadays it becomes manageable due to the arising developments and automation of LDV. The excitation in the measurements is carried out by means of an automated modal hammer in this work. While it is indeed cumbersome to re-position the hammer and to repeat the LDV scan, oftentimes one is only interested in a local excitation, e.g., in an excitation by a point or line force. In these cases, it is not necessary to excite the whole surface of the structure, since only certain columns of $\mathbf{Y}(\omega)$ are needed. Moreover, symmetry properties can also be exploited to reduce the measurement effort in many applications [\[19\]](#). Finally, we note that the proposed hybrid procedure is predominantly a low frequency method, and hence, coarse response and excitation grids are generally sufficient. Details on the experimental procedure for determining the mobility matrix $\mathbf{Y}(\omega)$ are reported for the test cases in [Sections 3.2 and 4](#).

2.1 Mesh coupling

The response and excitation grids need to be coupled to the BE mesh in order to exchange field quantities between the subdomains, see equations [\(3\)](#) and [\(5\)](#). The continuity, for example between the surface velocity \vec{v}_r of the structure and the fluid particle velocity v_f , can be expressed by the scalar equation

$$\vec{n} \cdot \vec{v}_r = v_f, \quad (6)$$

where \vec{n} is the normal vector on the surface pointing away from the acoustic domain. In the discrete setting, equation [\(6\)](#) can only be satisfied when the response points in the mobility measurement coincide with the interpolation nodes of the acoustic BE mesh. However, there are several reasons that support the use of nonconforming BE meshes: The appropriate resolution of the response grid in the experiment can be well anticipated based on the expected number of bending waves of the occurring structural modes. On the other hand, regarding BEM, there is no meshing guideline available in the context of coupled structural acoustic problems and hence, convergence studies are necessary in order to judge the appropriateness of a given BE discretization. Moreover, when coincidence occurs in the frequency range of interest, the acoustic mesh needs to be finer than the structural grid. A gradual refinement of a BE mesh in this context is computationally affordable in most cases. In contrast, repeating the mobility measurements on a finer grid is excessively

time-consuming if not prohibitive. The use of non-conforming meshes also allows the choice of different interpolation functions in the BE model.

When using non-conforming BE meshes, the continuity condition in equation [\(6\)](#) needs to be reformulated in a weak sense, i.e. [\[26\]](#)

$$\int_{\Gamma} \phi \vec{n} \cdot \vec{v}_r d\Gamma = \int_{\Gamma} \phi \mathbf{v}_f d\Gamma, \quad (7)$$

in which Γ denotes the submerged surface. Following a Bubnov–Galerkin approach, the test function ϕ is chosen as the interpolation function of the fluid domain. After discretization, equation [\(7\)](#) can be written in matrix form

$$\int_{\Gamma} \mathbf{N}_f^T \mathbf{n}^T \mathbf{N}_r d\Gamma \mathbf{v}_r = \int_{\Gamma} \mathbf{N}_f^T \mathbf{N}_f d\Gamma \mathbf{v}_f, \quad (8)$$

where \mathbf{N}_f and \mathbf{N}_r contain the interpolation functions associated with the BE mesh and the response grid in the experiment, respectively. Rearranging equation [\(8\)](#) yields the coupling matrix introduced in [\(5\)](#), i.e. [\[27\]](#)

$$\mathbf{C}_{fr} = \left[\int_{\Gamma} \mathbf{N}_f^T \mathbf{N}_f d\Gamma \right]^{-1} \int_{\Gamma} \mathbf{N}_f^T \mathbf{n}^T \mathbf{N}_r d\Gamma. \quad (9)$$

Note that the matrix in square brackets is also known as the boundary mass matrix Θ . Similar derivations are possible for the coupling matrix \mathbf{C}_{ef} , which was introduced in equation [\(3\)](#) to relate field quantities in the BE domain to the excitation grid.

The response and excitation grids used in the mobility measurements are defined respectively by subdividing the surface of the structure into quadrilateral elements. Both, response and excitation elements have shape functions which approximate the geometry of the surface. The nodes associated with those shape functions are denoted as geometrical nodes and they are located on the edges and boundaries of the element, i.e. neighboring elements share common geometrical nodes. Further, the above introduced interpolation functions contained in \mathbf{N}_r (and similarly those in \mathbf{N}_e for the excitation grid) establish a spatial approximation of field quantities. The associated nodes are called interpolation nodes. In the experiment, the structure under test needs to be excited at interpolation nodes of the excitation grid and the response needs to be measured at the interpolation nodes of the response grid. In order to avoid excitation and measurements on the edges and corners of the structure, interpolation nodes are placed inside the elements leading to discontinuous approximation of field quantities across element boundaries. In this work, quadrilateral elements with eight-noded, bi-quadratic geometry approximation and constant interpolation functions are used for the excitation and response grids. For the acoustic BE mesh, quadrilateral elements with nine-noded, bi-quadratic geometry approximation and discontinuous, bi-linear interpolation functions are employed. These elements are shown in [Figure 2](#).

The integral in equation [\(9\)](#) cannot be evaluated element-wise, since the interpolation functions of the response

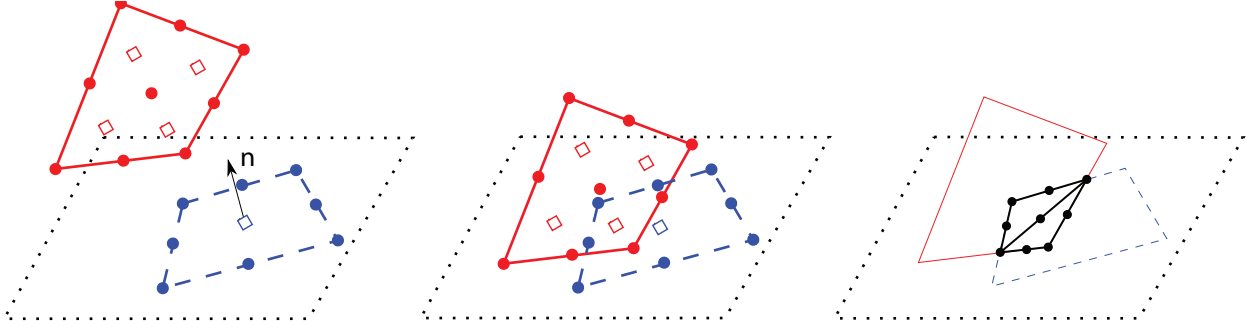


Figure 2. Schematic of the mortar projection of a master acoustic element (solid, red) onto the auxiliary plane (dotted) defined by an overlapping slave structural element (dashed, blue) and subsequent definition of triangular integration cells. Solid circles represent geometrical nodes and hollow squares represent interpolation nodes.

grid are not continuous across acoustic boundary elements and vice versa. This issue is overcome by a Mortar method [28], which works as follows: First, the acoustic boundary elements are defined as the master elements, and the elements on the response grid are defined as the slave elements, respectively, and pairs of overlapping elements are identified by a search algorithm. Then, an auxiliary projection plane and a corresponding normal vector are defined based on the slave element. The master element is then projected onto that plane, the resulting intersection area is subdivided into triangular elements, and integration is performed over them. The procedure is schematically depicted in Figure 2.

2.2 Diffuse field excitation

One of the main advantages of the proposed hybrid approach is the capability to experimentally determine the response to diffuse acoustic fields without unwanted effects associated with the measurement room. Usually, experimental characterization of structures subject to diffuse field excitation are conducted in reverberation rooms. These rooms need to be large enough in order to avoid modal behavior of the incident acoustic field, which is often an issue in the low frequency range. In contrast, application of incident acoustic fields in BEM only relies on accurate modeling of the scatterer's geometry.

There are three different approaches available to numerically predict the response to a diffuse acoustic field [29, 30]: (1) excitation by a set of random plane waves, (2) stochastic analysis based on power spectral densities (PSD), and (3) actual modeling of a large-enough reverberant room. Modeling a cavity that is large-enough to admit a diffuse sound field is computationally prohibitive when using a conventional BEM formulation. The approach based on PSD allows analytical modeling of the diffuse field but requires singular value decomposition and truncation of the PSD matrix in order to avoid inversion of fully populated BE matrices. But even with truncation of the PSD matrix, the plane wave approach, which was originally proposed by Rafaely [31], has been shown to be more efficient [29] and is thus followed here. The energy quantity of interest is computed as the average value among multiple simulations.

In each of those simulations, the structure is excited by a combination of N incident plane waves. The incident sound pressure $p^i(\vec{x})$ and corresponding particle velocity $v_f^i(\vec{x})$ at the interpolation node with the coordinate vector \vec{x} are obtained from

$$p^i(\vec{x}) = \frac{1}{\sqrt{N}} \sum_{i=1}^I \sum_{j=1}^J p_{i,j} e^{i(\vec{k}_{i,j} \cdot \vec{x} + \theta_{i,j})}, \quad \text{and} \quad (10)$$

$$v_f^i(\vec{x}) = \frac{1}{\sqrt{N}} \sum_{i=1}^I \sum_{j=1}^J \frac{p_{i,j}}{\rho c} \vec{n} \cdot \vec{k}_{i,j} e^{i(\vec{k}_{i,j} \cdot \vec{x} + \theta_{i,j})}. \quad (11)$$

The plane waves arrive from spatially uniformly distributed directions and are arranged on a semi-sphere. The corresponding wave vectors are given as

$$\vec{k}_{i,j} = \frac{\omega}{c} [\cos \alpha_i \sin \beta_j, \sin \alpha_i \sin \beta_j, \cos \beta_j]^T, \quad (12)$$

with $\alpha_i = i\pi/I$ and $\beta_j = 2j\pi/J$. Further, I is the integer value of $\sqrt{N\pi/4}$ and J is the integer value of $2I\sin\alpha_i$. Each of the N plane waves have a normally distributed amplitude $p_{(i,j)}$ and a random phase $\theta_{(i,j)}$.

2.3 Hybrid evaluation of radiation damping

The extent of radiation damping can be quantified either by modal loss factors, which are properties of the structural acoustic system, or by excitation dependent loss factors, which are a result of a harmonic response analysis [8]. Once the vibroacoustic response is evaluated by equations (1)–(5), the excitation dependent radiation loss factor for a specific frequency point is obtained via [32]

$$\eta_r = \frac{P}{|\omega E_{\text{tot}}|}. \quad (13)$$

The time-averaged radiated sound power P can be computed from the acoustic quantities via

$$P = \frac{1}{2} \text{Re}(\mathbf{p}^T \Theta \mathbf{v}_f^*), \quad (14)$$

where $(\cdot)^*$ denotes the conjugate complex and $\text{Re}(\cdot)$ refers to the real part of a complex quantity. The definition of the boundary mass matrix Θ was introduced in equation (9) and the paragraph thereafter. Note that the imaginary part of the complex sound power corresponds to near-field sound radiation, which has a mass-like effect on the structure and hence, does not dissipate energy.

For time-harmonic problems, the time-averaged total vibrational energy E_{tot} in equation (13) equals twice the time-averaged kinetic energy or alternatively, twice the time-averaged potential energy. The latter requires knowledge of the (static) stiffness matrix of the structure under test, which can not be estimated by mobility measurements. Instead, in the proposed hybrid procedure, we will compute the time-averaged total vibrational energy based on the kinetic energy of the structural acoustic system, i.e.

$$E_{\text{tot}} = \frac{1}{2} \mathbf{v}_r^T \left(\mathbf{M}_r - \frac{i}{\omega} \mathbf{C}_{\text{rf}} \mathbf{H}^{-1} \mathbf{G} \mathbf{C}_{\text{fr}} \right) \mathbf{v}_r^*, \quad (15)$$

in which the mass matrix \mathbf{M}_r of the structure under test is set up by estimating the structural mass contribution of each element on the response grid. For structures with uniform thickness and mass density, the mass contribution of each element is simply its area percentage times the total mass of the structure. Equation (15) also includes energy contributions of the fluid field, where the imaginary part of $\mathbf{H}^{-1} \mathbf{G}$ corresponds to the additional mass effect of the fluid, while the real part corresponds to the energy dissipated by sound radiation. A more elaborate discussion of equation (15) and the alternative way of evaluating the total energy are given in Appendix A.

3 Assessment of radiation damping of rectangular honeycomb sandwich panels

3.1 Set-up of the demonstrator

The set-up of the demonstrator is shown in Figure 3. A flat aluminum honeycomb sandwich panel is mounted onto a tub-shaped concrete foundation. The foundation has a square cross section of $0.8 \times 0.8 \text{ m}^2$, a height of 0.4 m and a vertically tapered wall thickness of around 0.06–0.1 m. The short edges of the rectangular panel are glued into aluminum F-profiles, which are then screwed onto the upper edge of the foundation. The long edges of the panel are not fixed and hence permit air flow between the two sides of the panel. The free length of the panel is approximately 0.750 m whereas two panel widths are studied. The studied panels are denoted with letters A and B, and their dimensions are given in Table 1. The material properties of aluminum and the honeycomb core are provided in Table 2. The concrete foundation is assumed to be rigid in this work.

3.2 Mobility measurements

The mobility matrix is determined by using an automated modal hammer (NV Tech SAM1 [33]), which allows to measure the exerted force by means of a force cell in the

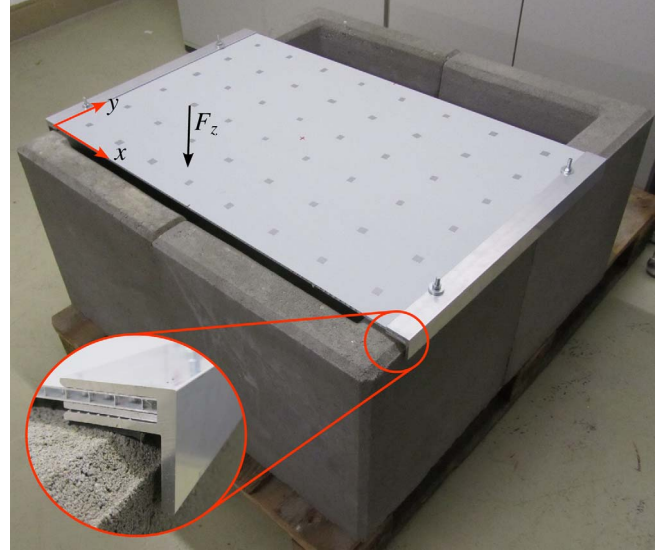


Figure 3. Set-up of the demonstrator including an aluminum honeycomb sandwich panel mounted onto a concrete foundation. The black arrow indicates the location of the point force introduced in Section 3.4.

hammer tip. The device is placed inside the concrete foundation using a flexible measurement stand allowing to position the hammer tip at the nodes of the excitation grids. A uniform excitation grid of 6×4 ($n_e = 24$) is used for panel A, and likewise 6×2 ($n_e = 12$) for panel B in order to derive the respective mobility matrices.

The velocity response is measured by means of scanning LDV using a single head Polytec PSV 500 system. The PSV 500 includes a camera for geometry alignment so that Euler compensation is applied to correct for the angle of laser beam incidence. Regarding the resolution of response grids, preceding (in-vacuo) modal analyses of the panels have been conducted with FEM in order to estimate the number of bending waves in the considered frequency range up to 625 Hz. Then, the response grids are defined such that a minimum of three elements capture one bending wave length. This corresponds to a response grid of 8×6 ($n_r = 48$) for panel A, and likewise 8×4 ($n_r = 32$) for panel B. The resulting mobility matrices $\mathbf{Y}(\omega)$ are of dimension 48×24 and 32×12 , respectively. Reflective tape is applied to the surfaces of the panels in order to improve the signal-to-noise ratio, see Figure 3. The velocity response is only measured on the top side of the panel and hence, the mobility data needs to be copied to the bottom side in order to couple the mobility matrix to the three-dimensional BE mesh. This approach is valid as long as the response of the panel only involves anti-symmetric bending motion, i.e. thickness deformation of the core does not occur, which is a reasonable assumption in the low frequency range.

The mobility matrix $\mathbf{Y}(\omega)$ is obtained by relating the measured velocities at the response nodes to the measured force at the excitations nodes. The corresponding transfer functions are evaluated based on a H_1 -estimator in the frequency range up to 625 Hz with a resolution of approximately 0.4 Hz. Rectangular window functions are applied

Table 1. Dimensions of aluminum honeycomb sandwich panels.

		Panel A	Panel B
Face sheet thickness, front	t_f	0.5 mm	0.5 mm
Face sheet thickness, back	t_b	0.5 mm	0.5 mm
Core thickness	h	3 mm	4.5 mm
Dimensions	$l_x \times l_y$	$0.752 \times 0.5 \text{ m}^2$	$0.748 \times 0.2 \text{ m}^2$

Table 2. Material properties of aluminum face sheets and aluminum honeycomb core.

Aluminum face sheets		
Density	ρ_f	2690 kg/m ³
Young's modulus	E	70 GPa
Poisson's ratio	ν_a	0.3
Aluminum honeycomb core		
Density	ρ_c	135 kg/m ³
Young's modulus	E_x, E_y	10 MPa*
Young's modulus	E_z	360 MPa
Shear modulus	G_{xy}	1 MPa*
Shear modulus	G_{yz}	280 MPa
Shear modulus	G_{xz}	140 MPa
Poisson's ratio	ν_c	0.01*

* Values that are not explicitly given by the manufacturer are

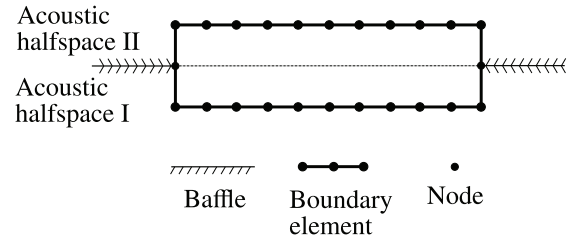
to the velocity as well as to the force signals in order to perform a fast Fourier transformation (FFT). The measurement time is large enough so that the signals die out within the window. All measurements are repeated ten times and complex frequency domain averaging is used to reduce the noise that is not phase correlated.

Although the mobility matrix $\mathbf{Y}(\omega)$ is subsequently coupled to different BE models representing the acoustic conditions (1)–(3), the actual measurement of $\mathbf{Y}(\omega)$ is conducted only once in a standard laboratory without absorbent treatments on the walls. This is a convenient choice and neglects the influence of the acoustic field on the structural response. This assumption will be justified later in Section 3.5, in which fully coupled FEM–BEM simulations are presented for the purpose of verification.

3.3 Boundary element models

As described in Section 2.1, the acoustic field around the panel is discretized by quadrilateral boundary elements with discontinuous bilinear interpolation functions. Uniform meshes with 36×24 elements along the in-plane directions of panel A, and 48×12 elements for panel B are employed. Moreover, the following three models for the acoustic domain are used in this work to study the effect of acoustic boundary conditions:

- Condition (1): The panel is assumed to be confined in an infinitely large acoustic baffle that prohibits flow between its two sides. Two independent acoustic subdomains on each side are modeled using a halfspace formulation with a modified Green's function [34]. This condition resembles the situation in a window

**Figure 4.** Cross-sectional schematic of a baffled panel modeled by two acoustic half-space BE meshes.

test rig. The corresponding BE model is schematically illustrated in Figure 4.

- Condition (2): The panel is assumed to be unbaffled and is situated in an acoustic full space. A single BE mesh with a closed surface is used. This condition resembles the situation in an anechoic chamber.
- Condition (3): The concrete foundation is additionally modeled. The sound waves radiated from the panel are scattered on the rigid surfaces of the foundation. A corresponding BE mesh of the foundation accommodating panel A is shown in Figure 8.

The numerals 1–3 after the alphabetical designation denote the considered configuration – e.g. panel A confined in a baffle will be referred to as panel A-1 in what follows.

3.4 Results obtained by hybrid procedure

This section studies radiation damping of the panels using the hybrid procedure described in Section 2. The focus is set on the influences of acoustic condition and excitation on radiation damping. The panels are excited by point forces, monopole sources and by diffuse incident fields. The point forces with magnitude of $F_z = 1 \text{ N}$ are located at $(x = 0.31 \text{ m}, y = 0.06 \text{ m}, z = h/2)$ of panel A, and likewise at $(x = 0.31 \text{ m}, y = 0.05 \text{ m}, z = h/2)$ of panel B. The coordinate system is defined such that the x -axis points in the direction of the long edges and the xy -plane coincides with the midplane of the panel, see Figure 3. The monopole sources are located at $(x = 1 \text{ m}, y = 0 \text{ m}, z = 0.3 \text{ m})$. The responses to diffuse incident fields are computed as the mean value of 300 sample simulations as described in Section 2.2. The excitation in each simulation is given by the summation of $N = 1145$ incident plane waves with normally distributed amplitudes with a mean value of 1 Pa and random phases. The convergence of the response to diffuse field excitation with respect to the number of sample simulations will be analyzed later in this section.

Figure 5 shows the experimentally determined point mobility of panel A. The corresponding radiated sound power and total power are plotted in Figure 6 for conditions (1)–(3). Those power quantities are computed using equations (14) and (15), and are later required to evaluate the extent of radiation damping. When comparing panels A-1 and A-2, we notice a considerable difference in radiated sound power in the low frequency range. This can be explained by the acoustic short circuiting occurring in panel A-2 (i.e. the panel with un baffled condition), which significantly reduces radiation efficiency. The difference in radiated sound power narrows with increasing frequency. The radiated sound power of panel A-3 (i.e. the panel with foundation) lies in between the curves of panels A-1 and A-2 for the most part of the considered frequency range, expect when cavity resonances occur inside the foundation. At the respective resonance frequencies, the radiated sound power of panel A-3 exhibits noticeable peaks that are marked with vertical dashed gray lines in Figure 6. The total power of the three panels shows only marginal differences, which arise due to the different BE matrices in the computation of the kinetic energy (cf. Eq. (15)). The structural velocity is the same for all three panels since the mobility measurement is only conducted once. A similar analysis based on a fully coupled FEM–BEM procedure will be presented in Section 3.5.

The resulting radiation loss factors are shown in Figure 7 for panels A and B in conditions (1)–(3). Sharp minima in the loss factors occur at the eigenfrequencies that are associated with bending modes in which sound pressure cancellation occurs between neighboring half-cells. This cancellation decreases in effect with increasing frequency. The baffled panels (A-2 and B-2) exhibit high radiation damping already in the low frequency range due to the first bending mode that radiates sound like a piston without cancellation. In contrast, the un baffled panels (A-1 and B-1) show much lower damping values due to the sound pressure cancellation at the edges, as already discussed in the context of Figure 6. As radiation efficiency increases with frequency, the curves converge to each other. Distinct maxima in radiation damping occur around the cavity resonance frequencies of panel A-3. They are related to the sound power peaks encountered in Figure 6. Note that panel B is only 200 mm wide and hence do not work as a closure of the tub-shaped foundation, which explains why this panel does not exhibit cavity resonances.

While the analysis in Figure 7 is limited to point force excitation, the main advantage of the proposed hybrid procedure is the capability to model excitation by incident acoustic fields. The procedure is illustrated in Figure 8 for panel A-3 at 145 Hz. First, an incident field with sound pressure \mathbf{p}_i is created and the resulting excitation force \mathbf{f}_i is computed by BEM via equation (4). Then, the structural response is evaluated via equation (1) using the experimental mobility matrix. Subsequent projection onto the BE mesh by equation (5) yields the fluid particle velocity. The latter only takes values on the panel, since the foundation is assumed to be rigid, see middle subplot in Figure 8. Finally, the complete sound pressure field \mathbf{p} is computed by

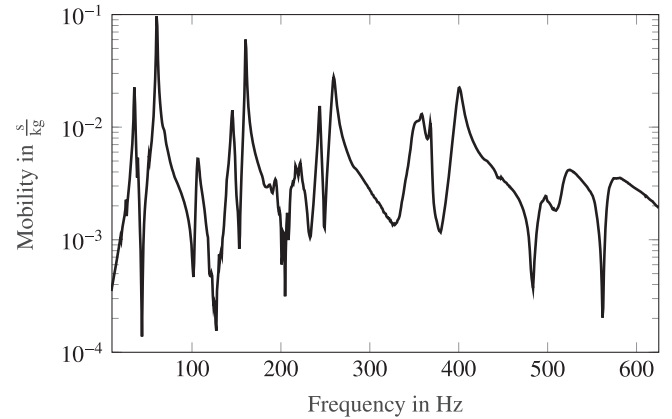


Figure 5. Measured point mobility of panel A at ($x = 0.31$ m, $y = 0.06$ m, $z = h/2$).

BEM and the radiation loss factor can be evaluated in a post processing step.

The radiation loss factors for diffuse field excitation are obtained by constructing multiple realizations of incident acoustic fields such as the one shown on the left subplot in Figure 8. The verification of this averaging approach is presented in Figure 9, which plots the mean value for the radiation loss factor of panel A-3 at 145 Hz with increasing number of incident field realizations. Each additional realization corresponds to a simulation with $N = 1145$ random incident plane waves. We notice that a number of 300 realizations is a reasonable compromise between computational effort and accuracy. This also holds for other frequency points and test cases in this work.

Figure 10 studies the excitation dependence of radiation damping. Loss factors for excitations by point forces, monopole sources and diffuse incident fields are shown. We notice significantly higher radiation damping when the panel is subject to incident acoustic fields. This can be explained by the spatially uniform distribution of the incident pressure field in the low frequency range that almost acts like a plane wave excitation. In frequency regions apart from the eigenfrequencies, this leads to a more uniform sound pressure distribution on the panel than is achieved by a point force excitation. At the eigenfrequencies however, radiation loss factors are expected to be independent of the excitation when the respective mode is (exclusively) excited. In that case, they are equal to the corresponding modal radiation loss factor [8]. This aspect is illustrated on the right subplot of Figure 10, in which all the structural resonance frequencies of panel B are marked with vertical dashed gray lines. We can observe that the loss factors for the three different types of excitation coincide at these frequencies. Note that a similar behavior is expected from panel A, but exceptions occur when the frequency resolution is too coarse, or when the respective mode is not exclusively excited.

The left subplot of Figure 10 shows extremely high radiation loss factors occurring around the cavity resonance frequencies of panel A-3. At 537 Hz, even $\eta_r = 1$ is approached, which indicates that almost all of the vibrational energy is

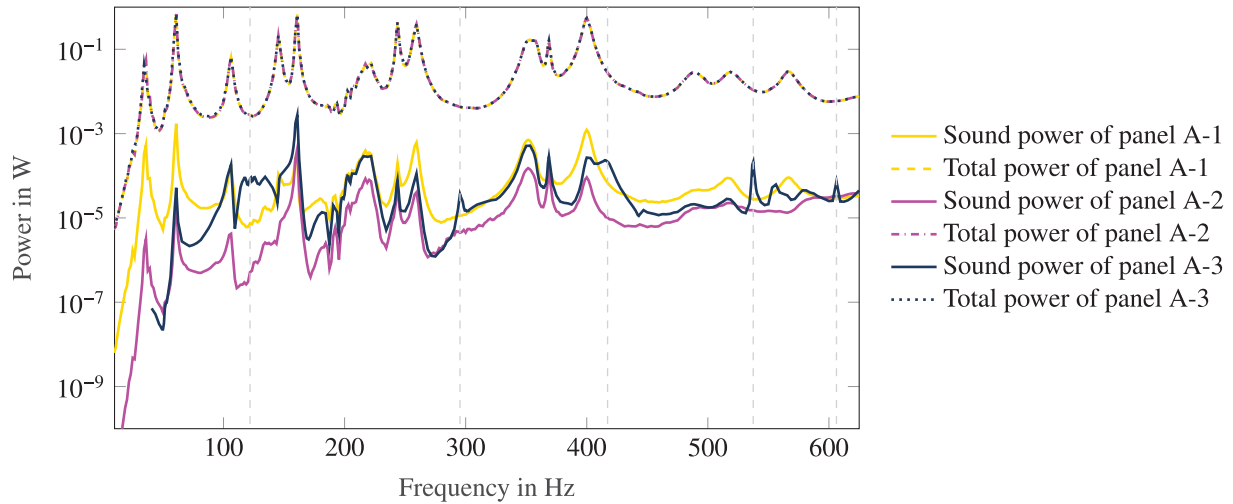


Figure 6. Radiated sound power and power corresponding to total vibrational energy of point-excited panel A evaluated by hybrid procedure. Vertical dashed gray lines indicate cavity resonances occurring in panel A-3.

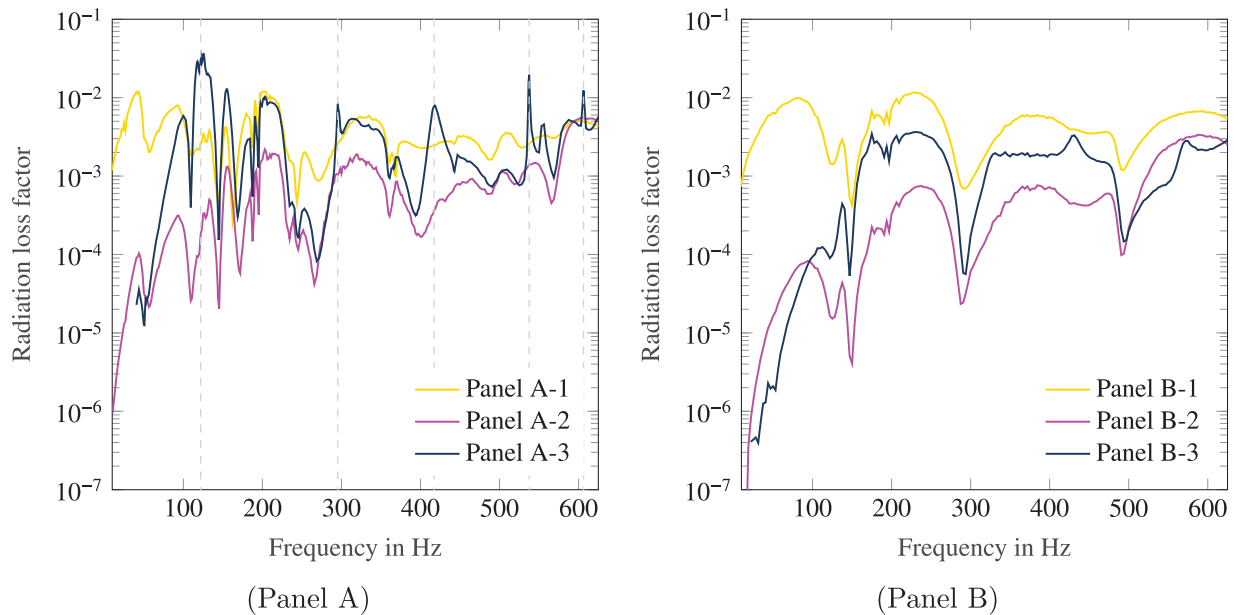


Figure 7. Radiation loss factors evaluated by hybrid procedure for point force excitation. Vertical dashed gray lines indicate cavity resonances occurring in panel A-3.

dissipated by sound radiation. This is a surprising result and requires further investigation in the future. It might be even possible to exploit the effect of (higher order) cavity resonances in order to deliberately dissipate vibrational energy by radiation damping.

3.5 Comparison to results obtained by coupled FEM–BEM procedure

The panels are now analyzed by a purely numerical FEM–BEM approach for the purpose of verification and comparison. The acoustic BE model is coupled to an FE model of the sandwich panel consisting of eight-noded quadrilateral shell elements based on the Reissner–Mindlin

theory for the representation of the face sheets and twenty-noded hexahedral solid elements for the core. The FE meshes of the panels comprise the same number of elements in the in-plane directions as the respective BE meshes. The mounting of the panels is modeled by constraining the translational DOFs along the center line of the short edges. Moreover, the relative displacement among the nodes on the short edges are also constrained in order to avoid unrealistic local deformation of the core. The FE modeling of the sandwich panels is schematically illustrated in Figure 11. A hysteretic loss factor of $\eta_s = 0.01$ is used in all upcoming simulations. While this is an assumed value, we note that structural damping has a negligible influence on radiation damping, as long as it is light and spatially homogeneous.

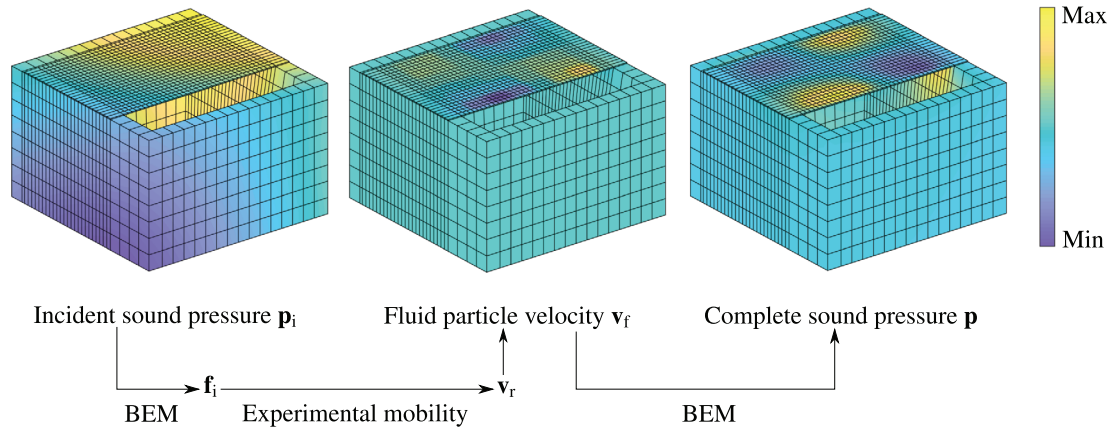


Figure 8. Hybrid procedure for evaluating the response to incident acoustic fields. The forcing vector corresponding to an incident acoustic field is computed by BEM. Then, the structural response is determined using the measured matrix of mobilities. Finally, the resulting acoustic field is computed by BEM. All subplots show the real parts of the respective complex-valued quantities.

Figure 12 shows the power quantities of panel A in conditions (1)–(3) subject to point force excitation at $(x = 0.31 \text{ m}, y = 0.06 \text{ m}, z = h/2)$. The results are computed by a fully coupled FEM–BEM procedure and are largely similar to the ones in Figure 6, which were obtained by the hybrid procedure. The only difference is that the FEM–BEM approach allows to include the reaction force due to the acoustic response and thus, capture the effect of acoustic conditions on the total vibrational energy. (Recall that the structural velocity was the same for all three acoustic conditions in the hybrid procedure, since the mobility measurement was only conducted once.) However, despite the mutual structural acoustic coupling, we only notice marginal differences in the total vibrational energy occurring in the vicinity of the resonance peaks, which are slightly shifted and rounded at higher frequencies due to the structural and acoustic damping contributions. This finding justifies that the mobility measurements reported in Section 3.2 were only conducted once per panel in a standard laboratory without absorbent treatments on the walls.

Figure 13 shows a comparison of diffuse field radiation loss factors obtained by the hybrid and the FEM–BEM procedure. We notice a good agreement across the whole frequency range for both panels. For panel B, even the resonance frequencies match the numerically predicted ones well with deviations ranging between 5% and 25%. This indicates that the simply supported boundary conditions in the FE model resembles the actual mounting condition with acceptable accuracy (cf. Fig. 3). Note that neither material properties nor the boundary conditions were “tuned” in the FE model in order to match the experimental results.

4 Assessment of radiation damping of a C-shaped aluminum sandwich panel

The second test case involves a C-shaped sandwich panel with a total thickness of 4 mm consisting of aluminum face sheets and a Polyethylen core. Due to prestress

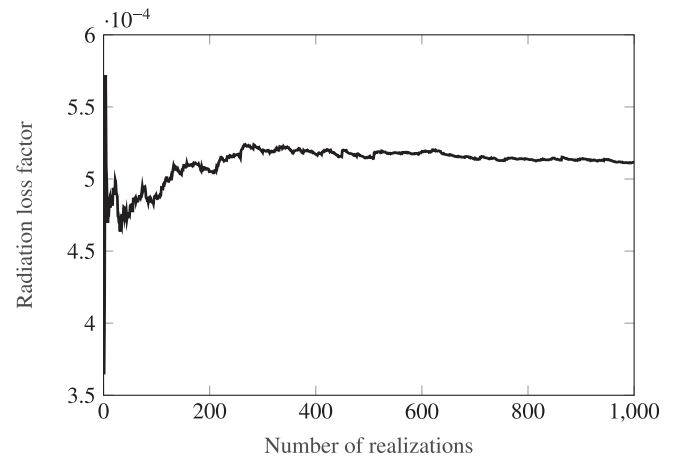


Figure 9. Mean value of the radiation loss factor of panel A-3 at 145 Hz with increasing number of random incident field realizations.

resulting from the bending of the panel during manufacturing, its elastic properties are subject to uncertainties, which makes the panel a suitable application for the proposed hybrid procedure. The set up is shown in Figure 14. The panel has a depth of 500 mm and a radius of 365 mm, which corresponds to an unfolded length of 1147 mm. Aluminum L-profiles are screwed onto the straight edges of the panel, which are then mounted onto the concrete foundation. The geometrical dimensions of the foundation were provided in Section 3.1. The material parameters of the unprocessed sandwich panel are listed in Table 3.

Only point force excitation is considered for this test case. The point force acts in radial direction and is located inside the C-shaped panel at an angular coordinate of approximately 0.13π and a distance of 100 mm from the edge in longitudinal direction. The excitation in the mobility measurement is again realized by a modal hammer that is positioned inside the concrete foundation (see Fig. 14). The velocity response in radial direction is measured by LDV, whereas the scanning process is divided into four runs

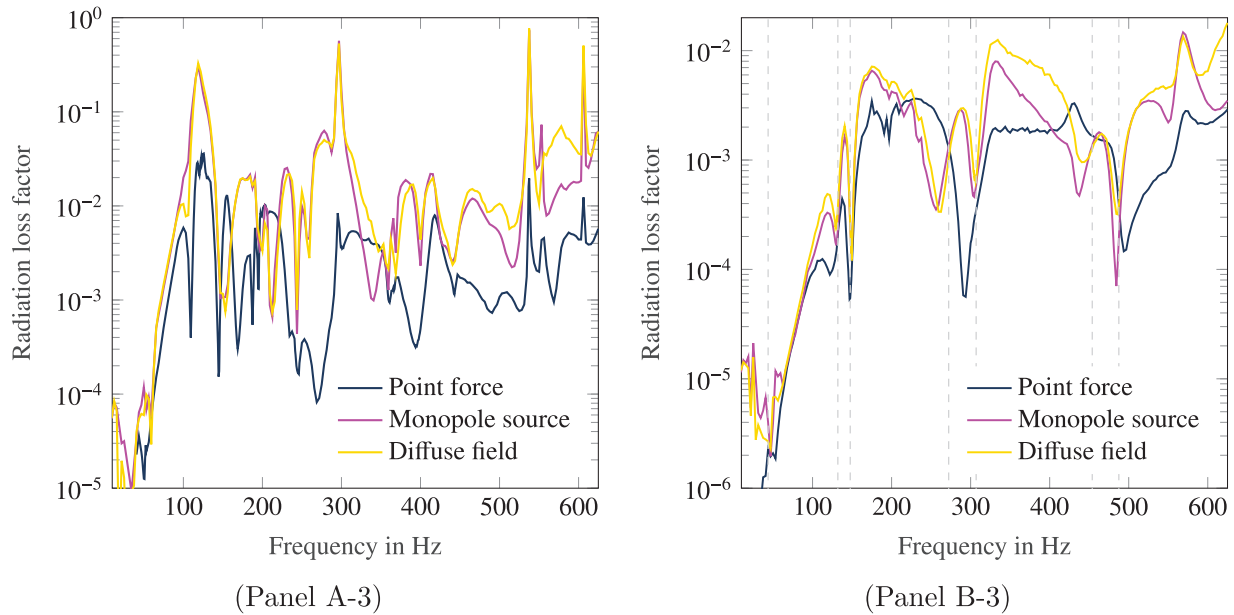


Figure 10. Radiation loss factors evaluated by hybrid procedure. Comparison among different types of excitation. Vertical dashed gray lines indicate structural resonances in panel B-3, at which the three loss factors are expected to coincide.

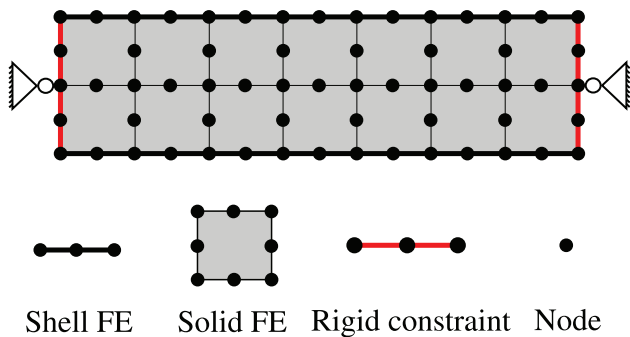


Figure 11. Cross-sectional schematic illustrating the FE modeling of a sandwich panel.

in order to ensure that all points on the response grid are well accessed by the laser. In each of the runs, the LDV is (re-)positioned and a $\pi/4$ arc of the surface is respectively measured. The force signal in the hammer is used as reference to retrieve phase information of all responses. Based on the anticipated structural modes, a uniform response grid of 5 points in longitudinal times 30 points in circumferential direction is employed, resulting in a total of $n_r = 150$ response points. The corresponding transfer functions are computed in the frequency range up to 375 Hz with a resolution of approximately 0.16 Hz. The frequency steps are smaller as compared to the test case in Section 3.2, since a longer measurement time was required to ensure that the signal has died out.

Acoustic radiation damping of the C-shaped panel is assessed by the proposed hybrid procedure. In this test case, only radiation into a free acoustic field is considered, and hence, the BE model only includes the panel but not the concrete foundation. No acoustic baffles are modeled either.

The BE mesh consists of 10 elements in longitudinal times 64 elements in circumferential direction. The resulting radiation loss factors are displayed in Figure 15. In addition, the loss factors obtained by the coupled FEM–BEM approach are also plotted. The underlying FE model of the sandwich panel is defined similar to ones described in Section 3.5 and comprises the same number of elements in the longitudinal and circumferential directions as the BE mesh.

In the considered frequency range, the C-shaped panel exhibits rather low radiation damping. The loss factors predicted by the hybrid and the purely numerical approach agree qualitatively with each other. Both of them indicate a gradual increase from $\eta_r = 10^{-5}$ to maximum values of around $\eta_r = 0.003$. However, we also notice significant differences, particularly around the dips at resonance frequencies. The latter are poorly predicted by the FE model, most likely due to the inadequate assumption of simply supported boundary conditions and due to prestress resulting from the bending of the panel during manufacturing. These findings encourage the use of the proposed hybrid procedure for an accurate assessment of radiation damping in the low frequency range under consideration of the actual mounting condition and realistic material properties.

5 Summary and conclusion

A hybrid experimental-numerical approach has been proposed for assessing acoustic radiation damping. The transfer functions characterizing the structural mobility are experimentally determined by means of automated hammer excitation on a grid and scanning LDV. Given the fact that radiation damping is particularly relevant in complex material configurations with a high ratio of bending stiffness to mass, this approach offers the advantage of

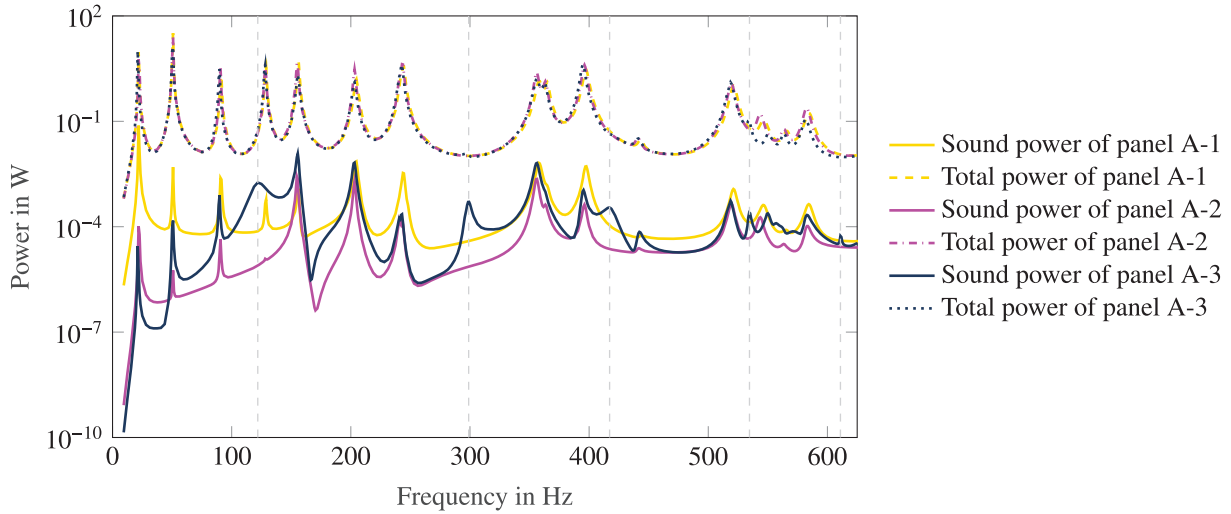


Figure 12. Radiated sound power and power corresponding to total vibrational energy of point-excited panel A evaluated by fully coupled FEM–BEM procedure. Vertical dashed gray lines indicate cavity resonances occurring in panel A-3.

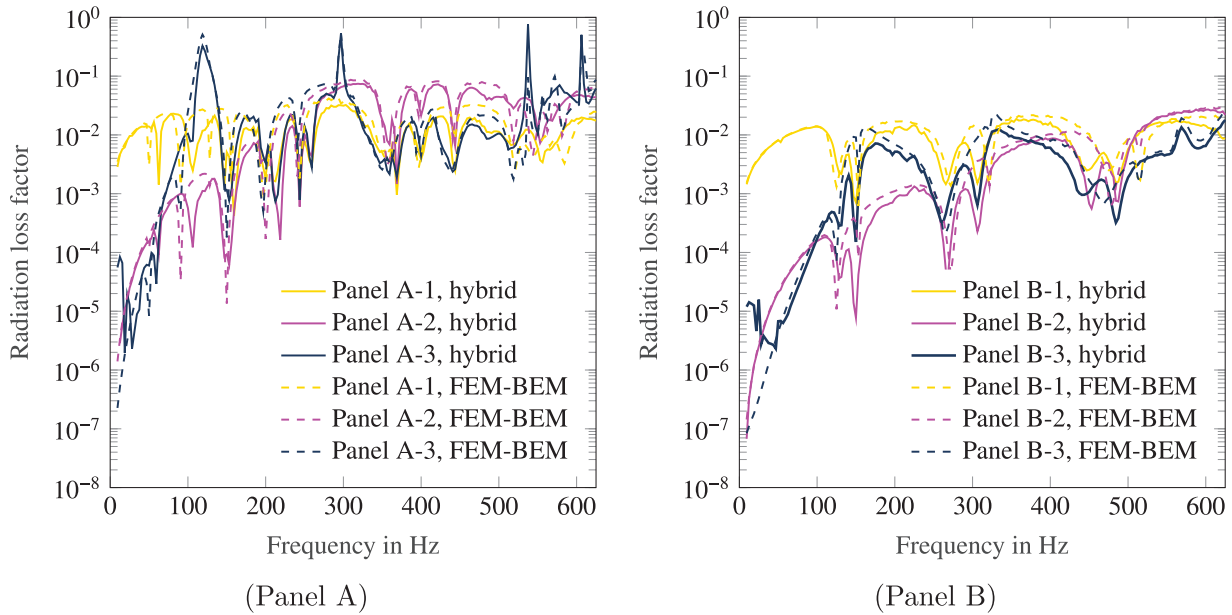


Figure 13. Radiation loss factors for diffuse field excitation. Comparison of hybrid approach to FEM–BEM procedure.

avoiding intricate constitutive modeling. Moreover, mobility measurements allow consideration of the actual mounting condition. The latter has a significant influence on the participating structural modes and thus radiation damping in the low frequency range.

While the structural behavior is characterized experimentally, the acoustic response that is needed for assessing radiation damping is computed by simulation. Thus, the limitations associated to acoustic measurements are avoided. The experimentally obtained matrix of mobilities is coupled to an acoustic BE model allowing to compute the response to diffuse acoustic fields even in the low frequency range. Moreover, the actual acoustic field can be modeled including the effect of acoustic short circuiting due to slits and gaps.

Rectangular aluminum honeycomb panels mounted onto a tub-shaped foundation served as demonstrator for verifying the proposed hybrid procedure. The structural mobilities of the panels were determined once and then coupled to various BE models resembling different acoustic conditions. The results illustrate that radiation damping is strongly dependent on the actual acoustic condition in the low frequency range. Moreover, using the same matrix of mobilities, radiation loss factors for excitation by point forces, monopole sources and diffuse incident fields were computed. Finally, radiation loss factors of a C-shaped panel were determined, in which the material properties are difficult to predict due to prestress. The findings underline the importance to properly consider mounting conditions, excitation and the actual acoustic field for an



Figure 14. Set up of the demonstrator including a C-shaped aluminum sandwich panel mounted onto a concrete foundation. A modal hammer inside the foundation provides the excitation for the mobility measurements. The red cross approximately indicates the point of excitation on the inside of the panel.

Table 3. Material properties of aluminum sandwich panel with Polyethylen core.

Aluminum face sheets		
Thickness	t	0.5 mm
Density	ρ_f	2690 kg/m ³
Young's modulus	E	70 GPa
Poisson's ratio	ν_a	0.3
Polyethylen core		
Thickness	h	3 mm
Density	ρ_c	1603 kg/m ³
Young's modulus	E_c	1 GPa*
Poisson's ratio	ν_c	0.1*

* Values that are not explicitly given by the manufacturer are assumed and marked with an asterisk.

accurate low-frequency assessment of radiation damping. Clearly, these demands can hardly be met by a purely experimental approach and thus, support the use of the proposed hybrid procedure.

Surprisingly high radiation loss factors were observed around the cavity resonance frequencies indicating that a large fraction of the vibrational energy is dissipated by sound radiation. This result requires further investigation in the future as it might open up new possibilities for exploiting radiation damping in order to deliberately dissipate vibrational energy.

Besides the assessment of radiation damping, this hybrid framework could also be used for evaluating sound transmission without the need of special facilities. This does not only include standard sound insulation measurements of partitions between two rooms. Further applications include the assessment of transmitted acoustic loading to the inside of transport vehicles. For example, space telescopes are subject to heavy acoustic loading during launch and typically carry vulnerable payloads such as cameras

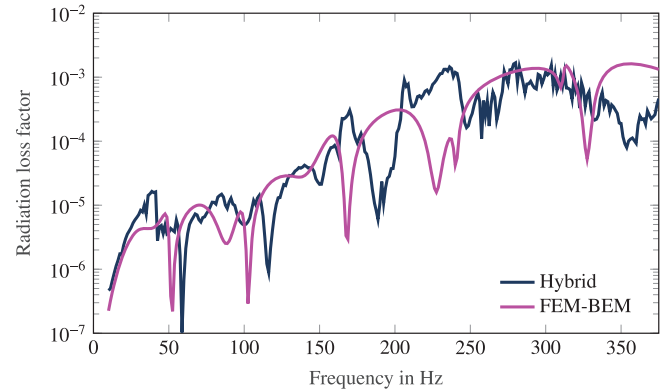


Figure 15. Radiation loss factor of the C-shaped aluminum sandwich panel subject to point force excitation. Comparison of hybrid approach to FEM-BEM procedure.

and scientific instruments. Often, the primary structures of spacecrafts also feature gaps and slits to address thermal expansion, which can hardly be addressed by purely acoustic measurements.

While we have briefly compared the results of the proposed hybrid approach to those obtained by a coupled FEM-BEM approach, proper benchmarking with respect to state-of-the-art experimental methods (e.g. ISO 3745) is an ongoing task.

Conflict of interest

The authors declare no conflict of interest.

Acknowledgments

This work was supported by the German Research Foundation (DFG project MA 2395/15-2) in the context of the priority program 1897 “Calm, Smooth and Smart – Novel Approaches for Influencing Vibrations by Means of Deliberately Introduced Dissipation”.

References

1. D.J. Mead: Passive vibration control, John Wiley & Sons Ltd, Chichester, England, 1999.
2. R.A. Mangiarotty: Acoustic radiation damping of vibrating structures. *Journal of the Acoustical Society of America* 35, 3 (1963) 369–377.
3. B.L. Clarkson, K.T. Brown: Acoustic radiation damping. *Journal of Vibration, Acoustics, Stress, and Reliability in Design* 107 (1985) 357–360.
4. O.P. Hentschel, M. Bonhage, L. Panning-von Scheidt, J. Wallaschek, M. Denk, P.A. Masserey: Analysis of an experimental setup for structural damping identification. *Journal of Theoretical and Applied Mechanics* 54, 1 (2016) 27–39.
5. R. Zhou, M.J. Crocker: Sound transmission loss of foam-filled honeycomb sandwich panels using statistical energy analysis and theoretical and measured dynamic properties. *Journal of Sound and Vibration* 329, 6 (2010) 673–686.

6. C. Scrosati, F. Scamoni, M. Bassanino, M. Mussin, G. Zambon: Uncertainty analysis by a round robin test of field measurements of sound insulation in buildings: single numbers and low frequency bands evaluation – airborne sound insulation. *Noise Control Engineering Journal* 61, 3 (2013) 291–306.
7. P. Bonfiglio, F. Pompoli: Numerical methodologies for optimizing and predicting the low frequency behavior of anechoic chambers. *Journal of the Acoustical Society of America* 134, 1 (2013) 285–291.
8. S.K. Baydoun, S. Marburg: Investigation of radiation damping in sandwich structures using finite and boundary element methods and a nonlinear eigensolver. *Journal of the Acoustical Society of America* 147, 3 (2020) 2020–2034.
9. M.J. Crocker, A.J. Price: Sound transmission using statistical energy analysis, *Journal of Sound and Vibration* 9, 3 (1969) 469–486.
10. K. Renji, P.S. Nair: On acoustic radiation resistance of plates. *Journal of Sound and Vibration* 212, 4 (1998) 583–598.
11. A. Billon, C. Foy, J. Picaut, V. Valeau, A. Sakout: Modeling the sound transmission between rooms coupled through partition walls by using a diffusion model. *Journal of the Acoustical Society of America* 123, 6 (2008) 4261–4271.
12. E. Reynders: Parametric uncertainty quantification of sound insulation values. *Journal of the Acoustical Society of America* 135, 4 (2014) 1907–1918.
13. A. Arjunan, C.J. Wang, K. Yahiaoui, D.J. Mynors, T. Morgan, V.B. Nguyen, M. English: Development of a 3d finite element acoustic model to predict the sound reduction index of stud based double-leaf walls. *Journal of Sound and Vibration* 333 (2014) 6140–6155.
14. C.W. Isaac, M. Pawelczyk, S. Wrona: Comparative study of sound transmission losses of sandwich composite double panel walls. *Applied Sciences* 10, 4 (2020) 1543.
15. M. Okuma: Low frequency noise and vibration analysis of boat based on experiment-based substructure modeling and synthesis, in *Vibro-Impact Dynamics of Ocean Systems and Related Problems*, R.A. Ibrahim, V.I. Babitsky, M. Okuma, Eds., Springer, Berlin, Heidelberg. 2009, pp. 203–214.
16. T. Tomatsu, T. Otsuka, M. Okuma, T. Okada, T. Ikeno, K. Shiomi: Sound-radiation analysis for boat hull based on hammering test and bem, in *Proceedings of ASME 2005 International Design Engineering Technical Conferences and Computers and Information in Engineering Conference*, September 24–28, 2005, Long Beach, California USA, pp. 259–264.
17. M. Shepherd, J.B. Fahnlne, T.P. Dare, S.A. Hambric, R.L. Campbell: A hybrid approach for simulating fluid loading effects on structures using experimental modal analysis and the boundary element method. *Journal of Acoustical Society of America* 138, 5 (2015) 3073–3080.
18. M. Xia, S. Li: A combined approach for active vibration control of fluid-loaded structures using the receptance method. *Archive of Applied Mechanics* 88 (2018) 1683–1694.
19. N.B. Roozen, Q. Leclère, D. Urbán, T. Méndez Echenagucia, P. Block, M. Rychtáriková, C. Glorieux: Assessment of the airborne sound insulation from mobility vibration measurements; a hybrid experimental numerical approach. *Journal of Sound and Vibration* 432 (2018) 680–698.
20. C.B. Goates, C.B. Jones, S.D. Sommerfeldt, J.D. Blotter: Sound power of vibrating cylinders using the radiation resistance matrix and a laser vibrometer. *Journal of the Acoustical Society of America* 148, 6 (2020) 3553–3561.
21. T.P. Bates, I.C. Bacon, J.D. Blotter, S.D. Sommerfeldt: Vibration-based sound power measurements of arbitrarily curved panels. *Journal of the Acoustical Society of America* 151, 2 (2022) 1171–1179.
22. S. Kirkup: The boundary element method in acoustics: a survey. *Applied Sciences* 9, 8 (2019) 1642.
23. N. Trompette, J.-L. Barbry, F. Sgard, H. Nelisse: Sound transmission loss of rectangular and slit-shaped apertures: experimental results and correlation with a modal model. *Journal of the Acoustical Society of America* 125, 1 (2009) 31–41.
24. T. Shimizu, Y. Kawai, D. Takahashi: Numerical analyses and experimental evaluation of reduction technique for sound transmission through gaps. *Applied Acoustics* 99 (2015) 97–109.
25. S. Marburg, B. Nolte: A unified approach to finite and boundary element discretization in linear time-harmonic acoustics, in *Computational Acoustics of Noise Propagation in Fluids. Finite and Boundary Element Methods*, S. Marburg, B. Nolte, Eds., Springer, Berlin, Germany. 2008, pp. 1–34.
26. A. de Boer, A.H. van Zuijlen, H. Bijl: Comparison of conservative and consistent approaches for the coupling of non-matching meshes. *Computer Methods in Applied Mechanics and Engineering* 197 (2008) 4284–4297.
27. H. Peters, S. Marburg, N. Kessissoglou: Structural-acoustic coupling on non-conforming meshes with quadratic shape functions. *International Journal for Numerical Methods in Engineering* 91, 1 (2012) 27–38.
28. B. Flemisch, M. Kaltenbacher, B.I. Wohlmuth: Elasto-acoustic and acoustic-acoustic coupling on non-matching grids. *International Journal for Numerical Methods in Engineering* 67, 13 (2006) 1791–1810.
29. P. Rong, M. Abele, O. von Estorff: Comparison of different methods for simulating acoustic diffuse field excitations. *Acta Acustica United with Acustica* 99 (2013) 931–939.
30. A. Panteghini, A. Feriani, E.A. Piana, N.B. Roozen: Evaluation of the sound reduction index of flat panels through FE models accounting for fluid-structure interaction: stochastic versus plane wave superposition methods. *Journal of Sound and Vibration* 509 (2021).
31. B. Rafaely: Spatial-temporal correlation of a diffuse sound field. *Journal of the Acoustical Society of America* 107, 6 (2000) 3254–3258.
32. F. Fahy, P. Gardonio: *Sound and structural vibration*, Academic Press, Oxford, United Kingdom, 2007.
33. P. Blaschke, T. Mallareddy, D. Alarcón: Application of a scalable automatic modal hammer and a 3D scanning laser doppler vibrometer on turbine blades, in *Proceedings of the 4th VDI conference in vibration analysis and identification*, VDI Berichte, vol. 2259, 2016.
34. M. Ochmann, H. Brick: Acoustical radiation and scattering above an impedance plane, in *Computational Acoustics of Noise Propagation in Fluids. Finite and Boundary Element Methods* S. Marburg, B. Nolte, Eds., Springer, Berlin, Germany. 2008, pp. 459–494.

Appendix A

Assessment of the total vibrational energy in coupled structural acoustic systems

The discretized equation of motion of a structural acoustic system, in which BEM is applied to the acoustic subdomain, reads

$$[\mathbf{K} - \omega^2 \mathbf{M} + i\omega \mathbf{C}_{\text{rf}} \mathbf{H}^{-1} \mathbf{G} \mathbf{C}_{\text{fr}}] \mathbf{u} = \mathbf{f}, \quad (16)$$

where \mathbf{u} is the unknown displacement vector, \mathbf{K} and \mathbf{M} are the structural stiffness and mass matrices, and \mathbf{f} is the excitation force. The matrix $i\omega \mathbf{C}_{\text{rf}} \mathbf{H}^{-1} \mathbf{G} \mathbf{C}_{\text{fr}}$ introduces additional mass and damping forces due to the acoustic field. Structural damping is neglected in the following.

As discussed in Section 2.3, the time-averaged total vibrational energy E_{tot} can be expressed as twice the time-averaged potential energy, i.e.

$$E_{\text{tot}} = \frac{1}{2} \mathbf{u}^T \mathbf{K} \mathbf{u}^* - \frac{1}{2} \mathbf{f}^H \mathbf{u}. \quad (17)$$

where the first term in equation (17) corresponds to the energy due to the elastic strain and the second term is the work done by external forces. In view of equation (16), it is obvious that E_{tot} may also be written as

$$E_{\text{tot}} = \frac{1}{2} \mathbf{u}^T (\omega^2 \mathbf{M} - i\omega \mathbf{C}_{\text{rf}} \mathbf{H}^{-1}(\omega) \mathbf{G}(\omega) \mathbf{C}_{\text{fr}}) \mathbf{u}^*, \quad (18)$$

which is equivalent to equation (15). When using e.g. FEM for modeling of the structural vibration [8], the evaluation of equation (17) is more favorable, since it does not involve fully populated BE matrices. All the necessary quantities including the stiffness matrix \mathbf{K} are readily available.

However, as discussed in Section 2.3, the situation is different when characterizing the structural behavior by mobility measurements. In that case, it is not possible to estimate the (static) stiffness matrix \mathbf{K} , and the approach in equation (18) is more appropriate. Finally, we note that the expressions in equations (17) and (18) are not fully equivalent to each other when structural damping contributions are considered.

Cite this article as: Baydoun SK, Roozen NB, & Marburg S. 2022. Hybrid assessment of acoustic radiation damping combining in-situ mobility measurements and the boundary element method. Acta Acustica, 6, 44.